Numerical analysis of natural convection with conjugate heat transfer in coarse-grained porous media

Chakkingal, Manu; Kenjereš, Saša; Ataei-Dadavi, Iman; Tummers, M. J.; Kleijn, Chris R.

Important note
To cite this publication, please use the final published version (if applicable).
Please check the document version above.

Numerical analysis of natural convection with conjugate heat transfer in coarse-grained porous media

Manu Chakkingal[a,*], Saša Kenjereš[a], Iman Ataei-Dadavi[a], M.J. Tummers[b], Chris R. Kleijn[a]

[a]*Transport Phenomena Section, Department of Chemical Engineering, Delft University Of Technology, Delft, The Netherlands*
[b]*Fluid Mechanics Section, Department of Process and Energy, Delft University Of Technology, Delft, The Netherlands*

Abstract

We report numerical simulations of fluid natural convection with conjugate heat transfer in a bottom-heated, top-cooled cubical cavity packed with relatively large ($d/L = 0.2$) solid spheres in a Body Centered Tetragonal (BCT) configuration. We study largely varying solid-to-fluid thermal conductivity ratios between 0.3 and 198, for a fluid Prandtl number of 5.4 and fluid Rayleigh numbers between 1.16×10^6 and 1.16×10^8 and compare global heat transfer results from our present simulations to our previously published experimental results. The interplay between convection suppression due to the solid packing, and conductive heat transfer in the packing leads to three different regimes, each with a distinct impact of the solid packing on the flow and heat transfer. At low Rayleigh numbers $\approx 10^6$, all packings suppress convective flow. Compared to fluid only Rayleigh-Bénard convection, heat transfer is therefore reduced in low conductivity packings, whereas for high conductivity packings it is increased due to significant conductive heat transfer. At intermediate Rayleigh numbers $\approx 10^7$, low conductivity packings no longer suppress convection, whereas flow is still suppressed in high conductivity packings due to the thermal stratification imposed on the fluid by the solid. Consequently, heat transfer is lower compared to fluid only Rayleigh-Bénard convection, even in high conductivity packings. With a further increase of Rayleigh number $\gtrsim 10^8$, convection starts to be the dominant heat transfer mechanism in all packings, and convective heat transfer is close to that for fluid only Rayleigh-Bénard convection. The contribution of solid conduction in high conductivity packings causes the overall heat transfer to be above that for Rayleigh-Bénard convection.

Keywords: Natural convection, Porous media, Local temperature distribution, Local fluid flow, Structured packing, Laminar-Oscillatory flow

1. Introduction

The study of convective heat transfer in porous media has been mostly based on Darcy's model for porous media, i.e. an approach in which porosity is accounted for in a volume-averaged sense. It assumes that the porous length scales are small compared to the flow and thermal length scales. In various practical applications, such as convection in gravel embankments [1], in heat exchangers [2], in packed bed reactors [3], in fins to enhance heat transfer [4] or in the hearth of blast furnaces [5], however, the porous material is coarse-grained, i.e. the porous length scales are not small compared to the dimensions of e.g. hydrodynamic and thermal boundary layers and thermal plumes.

Detailed studies on the approaches and challenges in modelling variable density flows in porous media reported in [6, 7] explain the use of the standard Darcy model and various extended Darcy models (such as the Darcy-Forscheimer model, which accounts for high-Reynolds number effects). All these models are based on the volume averaging approach, and, although not providing information on flow and thermal features at the pore-scale, these studies help us in understanding the global flow and heat transfer in porous media.

Numerical studies with both standard [8] and extended [9] Darcy models using a local thermal equilibrium assumption, where a single equation is used to describe the temperature in the fluid, as well as the porous medium, discuss the effects of particle size and thermal properties in heat transfer. They suggest that the critical Rayleigh number for the onset of convection predicted with the Darcy-Forscheimer model decreases from the value predicted by the standard Darcy flow model, as the particle diameter and/or the liquid-to-solid conductivity ratio is increased. The intensity of the convective flow is also reported to depend on the Darcy number Da and the fluid Prandtl number Pr_f. A Da independent asymptotic convective heat transfer regime is reported at higher Ra_f. Using separate energy equations for the solid and fluid regions have been reported [10] to lead to better predictions of overall heat transfer compared to the local equilibrium approach.

Whereas solid conduction may play an important role in the heat transfer in porous media at low Ra_f, convective heat transfer becomes increasingly dominant with increasing fluid Rayleigh number Ra_f [11, 12]. These experimental results calculate the thermal boundary layer thickness from the Nusselt number. The increase in Nusselt number with the thinning of thermal boundary layer hints at the increased contribution of

---

*Corresponding author
Email address: `M.Chakkingal@tudelft.nl` (Manu Chakkingal)

Nomenclature

Greek Symbols

α	Thermal diffusivity, $(\lambda/\rho c_p)$, m^2/s
β	Coefficient of volume expansion of fluid, K^{-1}
λ	Thermal conductivity, W/m.K
ν	Kinematic viscosity of fluid, m^2/s
ϕ	Porosity
ρ	Density of fluid, kg/m^3

Abbreviations

$\mathbf{u}^*$	non-dimensional pore-scale velocity, $\dfrac{\mathbf{u}}{U_0}$
$\mathbf{u}$	Pore-scale velocity, m/s
$\mathbf{g}$	accel. due to gravity (acts along Z axis), m/s^2
Θ^*	Non-dimensional temperature, $\dfrac{T - T_c}{T_h - T_c}$
c_p	Specific heat capacity, J/kg.K
d	Diameter of sphere, m
Da	Darcy number, K/L^2
E	Effective heat transfer *w.r.t* RB convection
E_{conv}	Effective convective heat transfer *w.r.t* RB convection
K	Permeability
L	Height of cavity, m
Nu_f	Nusselt number based on fluid properties

Nu_c	Non-dimensional heat transfer due to conduction in the porous media filled cavity
Nu_{RB}	Nusselt number Rayleigh-Bénard convection
p	Pressure, N/m^2
Pr	Prandtl Number
Ra_f	Rayleigh Number based on fluid properties, $\dfrac{\mathbf{g}\beta_f \Delta T L^3}{\nu_f \alpha_f}$
T	Temperature, K
T_{ref}	Reference temperature, $\dfrac{T_h + T_c}{2}$, K
t_0	characteristic time scale, $\dfrac{L}{U_0}$, s
U_0	characteristic velocity scale, $\dfrac{Ra_f{}^{3/7}\alpha}{L}$, m/s
X, Y, Z	represents the rectangular coordinate system
PP	Polypropylene
RB	Fluid only Rayleigh-Bénard convection

Subscripts

c	Cold
f	Fluid
h	Hot
n	Normal to the surface
s	Solid

convective flow in the heat transfer process. Considerable scatter in experimental data, however, is reported at moderate Ra_f. Visualization of the flow at the upper boundary of a porous media filled, bottom-heated cavity [13] shows an increase in lateral spread of the fluid velocity, suggesting an increase in the 3-dimensionality of the flow within the pore-space at higher Ra_f. Indeed, our recent particle image velocimetry experiments [14] in a bottom heated cavity packed with optically transparent hydrogel beads show an increase in flow velocities within the pore-space with an increase in Ra_f. However, the results from the experiments are limited to a 2D plane due to the complex geometry.

Studies on convection in cavities filled with comparatively coarse-grained porous media, such as packed beads [15], suggest the use of effective (i.e. volume averaged, combined for fluid and solid) medium properties to explain the heat transfer mechanism. Heat transfer measurements in different fluids and in porous media consisting of beads of different conductivity and size, for instance, could be adequately quantified in terms of the effective Prandtl number of the porous medium. The overall heat transfer is reported to be independent of the

fluid Prandtl number Pr_f when the effective Prandtl number of the medium is high. Similar studies on heat transfer in metal foams also report the influence of Ra_f and Da on heat transfer [16, 17].

However, in contrast to what is found in [15], for porous media like metal foams, it is reported [10, 18] that non-dimensional numbers calculated from effective medium properties are insufficient to fully characterize natural convective heat transfer. Studies on the influence of the shape and morphology of the solid structures in porous media [19] show that heat transfer depends on the specific surface area of the porous medium, further illustrating the need to analyse convective heat transfer in (coarse-grained) porous media while addressing local, 3-dimensional, pore-scale effects, rather than effective media properties alone. Such local information helps in understanding global heat transfer mechanisms [12], and is essential for the development and evaluation of Volume Averaged Navier Stokes (VANS) closure models for convective flow in such media [20, 21].

At present, a detailed study accounting for pore-scale flow and thermal effects in coarse-grained porous media is missing in

the literature. In this paper, we present a detailed 3D numerical study, resolving the local convective flow and temperature distributions in coarse-grained porous media with conjugate heat transfer. This paper aims at understanding the heat transfer process in a bottom heated cubical cavity filled with a structured packing of relatively large spheres of varying conductivity, and teaches that the interplay between convection suppression due to the solid packing, and conductive heat transfer in the packing, leads to three different convection regimes, each with a distinct impact of the solid packing on the flow and heat transfer.

2. Mathematical formulations and numerical methods

2.1. Physical Problem

Natural convection in porous media is analysed in a bottom-heated, top-cooled cubical cavity with dimensions $L \times L \times L$ at fluid Rayleigh numbers, in the range $1.16 \times 10^6 \leq Ra_f \leq 1.16 \times 10^8$. The porous medium is composed of spherical beads arranged in structured Body Centred Tetragonal (BCT) Packing. The ratio of the diameter of the beads, d to the length of the cavity, L is chosen to be 0.2. Due to the finite dimensions of the cavity, the average porosity is $\phi = 0.41$ (as opposed to $\phi = 0.302$ for an infinite BCT packing) and estimating the permeability from the Kozeny–Carman equation, $K = \frac{\phi^3 d^2}{180(1-\phi)^2}$ [22], we get $Da \sim 4 \times 10^{-5}$. Water is used as the fluid ($Pr_f = 5.4$). Various materials are studied as packing materials, resulting in solid-to-fluid thermal conductivity ratios between 0.3 and 198. As will be discussed later, the cases studied in this paper lead to stationary or slightly oscillatory laminar flows in the porous media filled cavity. With $\beta \sim 2 \times 10^{-4} \text{K}^{-1}$ and $\Delta T < 10\text{K}$, it is ensured in all our simulations that $\beta \Delta T << 1$ and thus the Boussinesq approximation is valid. Using the Boussinesq approximation [23], we numerically solve the transient Navier-Stokes and thermal energy transport equations for Newtonian flow and conjugate heat transfer in and between the fluid and the solid.

Fluid phase:

$$\nabla \cdot \mathbf{u} = 0 \tag{1}$$

$$\frac{\partial \mathbf{u}}{\partial t} + \mathbf{u} \cdot \nabla \mathbf{u} = -\frac{1}{\rho} \nabla p + \nu \nabla^2 \mathbf{u} + \mathbf{g} \beta (T_f - T_{ref}) \tag{2}$$

$$\frac{\partial T_f}{\partial t} + \mathbf{u} \cdot \nabla T_f = \alpha_f \nabla^2 T_f \tag{3}$$

Solid phase:

$$\frac{\partial T_s}{\partial t} = \alpha_s \nabla^2 T_s \tag{4}$$

For used symbols, we refer to the List of Nomenclature.
The solid and fluid regions are coupled via Dirichlet–Neumann Partitioning. The fluid region is solved with the Dirichlet boundary condition $T_f = T_s$ at the coupled interface, while the solid region is solved with Neumann boundary condition:

$$\lambda_f \frac{\partial T_f}{\partial n} = \lambda_s \frac{\partial T_s}{\partial n} \tag{5}$$

calculated locally. The fluid and solid regions are solved iteratively.

2.2. Numerical Method

In order to perform numerical simulations in our present complex geometry, we make use of the capabilities of the Open-FOAM finite volume CFD solver [24]. We use unstructured tetrahedral grids to carry out numerical simulations for the packed bed cavities and structured grids for the reference (fluid only) Rayleigh-Bénard convection simulations (further referred to as RB convection). The application and accuracy of OpenFOAM in using arbitrary tetrahedral meshes has been scrutinized in [25], who conclude that differences between the solutions with unstructured tetrahedral grid cells and non-body conforming cartesian grids are small, but with additional computational costs for simulations with tetrahedral grids. The capability of Open-FOAM to accurately simulate momentum and mass transfer using unstructured grids are also discussed in [26, 27].

The above set of equations, Eq.(1)-(4) are thus discretized and fully resolved numerical simulations are carried out, using a conjugate heat transfer solver that we developed in Open-FOAM 2.4.0 [24]. The standard solver "chtMultiRegionFoam" in OpenFOAM is modified to account for the Boussinesq approximation as implemented in the standard solver "buoyant-BoussinesqPimpleFoam". The temperature equation for the solid phase is treated as a passive scalar equation. In Appendix A we present a detailed validation study for our newly developed solver against two literature studies [28, 29] on conjugate heat transfer in natural convection. In the simulations reported below, we use a 2nd order backward differencing time marching scheme and a 2nd order central differencing scheme defined as "backward scheme" and "limitedLinear" respectively in Open-FOAM to solve the convective and diffusive terms for both the solid and fluid phase [24]. The pressure-velocity-coupling at each time step is handled by the iterative PISO algorithm [30]. The energy transport equation (Eq.(3)) is solved with the divergence-free velocity obtained in each time step.

2.3. Geometry and Boundary conditions

We use water as the working fluid and study a range of fluid Ra_f ($1.16 \times 10^6 \leq Ra_f \leq 1.16 \times 10^8$). The material of the BCT packed beads is varied to realize a large variation in solid-to-fluid thermal conductivity ratios, viz. $\lambda_s/\lambda_f = 0.3$ for polypropylene, 1.0 for hydrogel, 70 for steel and 198 for brass, respectively. The coordinate system is chosen such that gravity, $\mathbf{g}$ acts along Z axis. The bottom and top walls are isothermal at temperatures T_h and T_c ($T_h > T_c$) respectively. All vertical walls of the cavity are adiabatic. No-slip boundary conditions are applied at all walls.

A grid independence study is carried out using three different meshes. In all the simulations reported, the flow was found to be in the laminar regime, with slight oscillations at the highest Ra_f reported. Thus the global non-dimensional heat transfer at the walls, defined by the Nusselt number, was chosen as the criterion to check grid independence. On the coarsest mesh 1, a fixed tetrahedral grid cell size $h \approx d/8 \approx L/40$ was used in the solid phase and in the core of the cavity, and consequently also at the interfaces between the fluid and the solid spheres. Along the isothermal walls, the grid cell size

was gradually refined to $h_{BL} \approx d/16 \approx L/80$. For the medium mesh 2 we used $h \approx d/12 \approx L/60$ and $h_{BL} \approx d/16 \approx L/80$, whereas for the finest mesh 3 we used $h \approx d/16 \approx L/80$ and $h_{BL} \approx d/32 \approx L/160$. At the highest studied Rayleigh number $Ra_f = 1.16 \times 10^8$, the deviation in overall Nusselt number obtained between mesh 2 and mesh 3 is found to be less than 3%. Consequently, the mesh 3 is used for all presented simulations, i.e. with a base grid size $h \approx d/16$, refined to $h_{BL} \approx d/32$ in the thermal boundary layers along the isothermal walls. The latter is in line with the recommendation $h_{BL}/L \approx 0.75 Nu_f^{-3/2}$ [31] and experimentally obtained values for Nu_f [14], and ensures a minimum number of 5-6 cells in the wall thermal boundary layers. The resulting mesh consists of $\sim 5 \times 10^6$ non-uniform tetrahedral grid cells. Because of the laminar flow characteristics varying from pure steady to slightly oscillatory, an adaptive time stepping is specified such that the Courant-Friedrichs-Lewy number is below 0.33. In practice, this led to a fixed simulation time step once a quasi-steady state had been reached.

3. Results and Discussion

3.1. Instantaneous thermal field features

To illustrate the influence of the solid-to-fluid thermal conductivity ratio on the temperature distribution in the cavity, Fig.1 shows side views of the thermal plumes (projected in the XZ-plane) at $t/t_0 = 20$ for a cavity packed with hydrogel (top) and brass beads (bottom) (solid-to-fluid thermal conductivity ratio of 1 and 198, respectively). The thermal plumes are identified as the isosurfaces of the instantaneous non-dimensionalized temperature $\Theta^* = 0.8$ [hot (red)] and 0.2 [cold (blue)] at $t/t_0 = 20$. In the brass packed cavity, at $Ra_f = 1.16 \times 10^7$, the thermal plumes are confined to a height less than the first layer thickness of the beads. In a cavity packed with hydrogel beads, on the other hand, cold and hot plumes meandering through the void space in the packing result in convective flow throughout the domain. At $Ra_f = 1.16 \times 10^8$, the thermal plumes meander and penetrate the pore spaces within the bulk of the porous medium as well as along the side walls, for both brass and hydrogel packings. Compared to $Ra_f = 1.16 \times 10^7$, we see a thinning of the thermal plumes at $Ra_f = 1.16 \times 10^8$. Such plume thinning at higher Ra_f was also observed in our experimental study [14].

The nature of the flow structures is visible in Fig.2, showing instantaneous $u - w$ velocity vectors at $t/t_0 = 20$, in a characteristic vertical plane located at $Y/L = 0.62$. At $Ra_f = 1.16 \times 10^7$ (Fig.2), the flow is mainly localized along the side walls for brass packing. The horizontally stratified temperature distribution confirms the absence of prominent flow in core of the cavity. The flow structures change with the conductivity of the solid packing material. For low conductivity hydrogel packing, the flow is no longer localized along the side walls, but also prevalent throughout the cavity, with a comparatively weaker flow in the core of the cavity. This has a strong impact on the temperature distribution. At $Ra_f = 1.16 \times 10^8$ (Fig.2), on the other hand, fluid flow is present throughout the cavity for both brass and hydrogel packings, as reflected in the temperature contours.

The local Nusselt number, Nu_f calculated as:

$$Nu_f = -\frac{L}{\Delta T}\left(\frac{\partial T}{\partial y}\right)_{wall} \quad (6)$$

where, ΔT and L are the temperature difference and distance between the hot and cold walls respectively, is analyzed at the hot wall to understand the influence of the packing material on heat transfer. The presence of coarse-grained porous media results in strong local variations of the (instantaneous) Nusselt number Nu_f along the isothermal walls, depending on the thermal conductivity of the packing material (Fig.3). For a high conductivity brass packing and low $Ra_f = 1.16 \times 10^7$, local high Nu_f spots occur close to the point of contact of the spheres with the wall, due to the dominance of solid conduction over convective heat transfer in these points. At higher $Ra_f = 1.16 \times 10^8$, the contribution of convective heat transfer relative to solid conduction increases, and heat transfer becomes more uniform and higher on average.

For a low conductivity hydrogel packing and low $Ra_f = 1.16 \times 10^7$, high Nu_f regions occur mostly close to the side walls, due to the dominance of convective heat transfer in these regions. On average, however, heat transfer is lower than for brass packing. At higher $Ra_f = 1.16 \times 10^8$, convective heat transfer enhancement is no longer limited to the near wall regions, and heat transfer is more uniform along the entire isothermal wall. Although distributed differently along the wall, at $Ra_f = 1.16 \times 10^8$ the average heat transfer is dominated by convection and similar for both low and high conductivity packing.

3.2. Instantaneous flow feature analysis

The instantaneous velocities ($\mathbf{u}$) are non-dimensionalized with characteristic velocity scale (U_0) [1] [32], such that the non-dimensional velocity vector $\mathbf{u}^*$ equals

$$\mathbf{u}^* = \frac{\mathbf{u}}{U_0}$$

In Fig.4, the vertical flow in the packed cavity is visualized by means of isosurfaces of the non-dimensional vertical velocity w^* being 0.2 (red) and -0.2 (blue) at $t/t_0 = 20$. At $Ra_f = 1.16 \times 10^7$, vertical flow is virtually absent in the case of a brass packed cavity, while in the hydrogel packed cavity a relatively strong vertical flow is present close to the side walls, with a weaker flow in the core of the cavity. At $Ra_f = 1.16 \times 10^8$, relatively strong vertical flows are present along the side walls as well as in the core of the cavity, both in brass and in hydrogel packed cavities. The flow in the core of the cavity is stronger in the case of a hydrogel packed cavity, compared to the brass packed cavity.

What was observed for the vertical velocity component, is also generally seen for the lateral velocity components. Fig.5

---

[1] The convective velocity scale is calculated as:

$$U_0 = \frac{Ra_f^{3/7}\alpha}{L}$$

which follows from, $U_0 = \frac{\mathbf{g}\beta\Delta\mathbf{T_f}\delta_\theta^2}{\nu_f}$ where, $\delta_\theta = Ra_f^{-2/7}L$
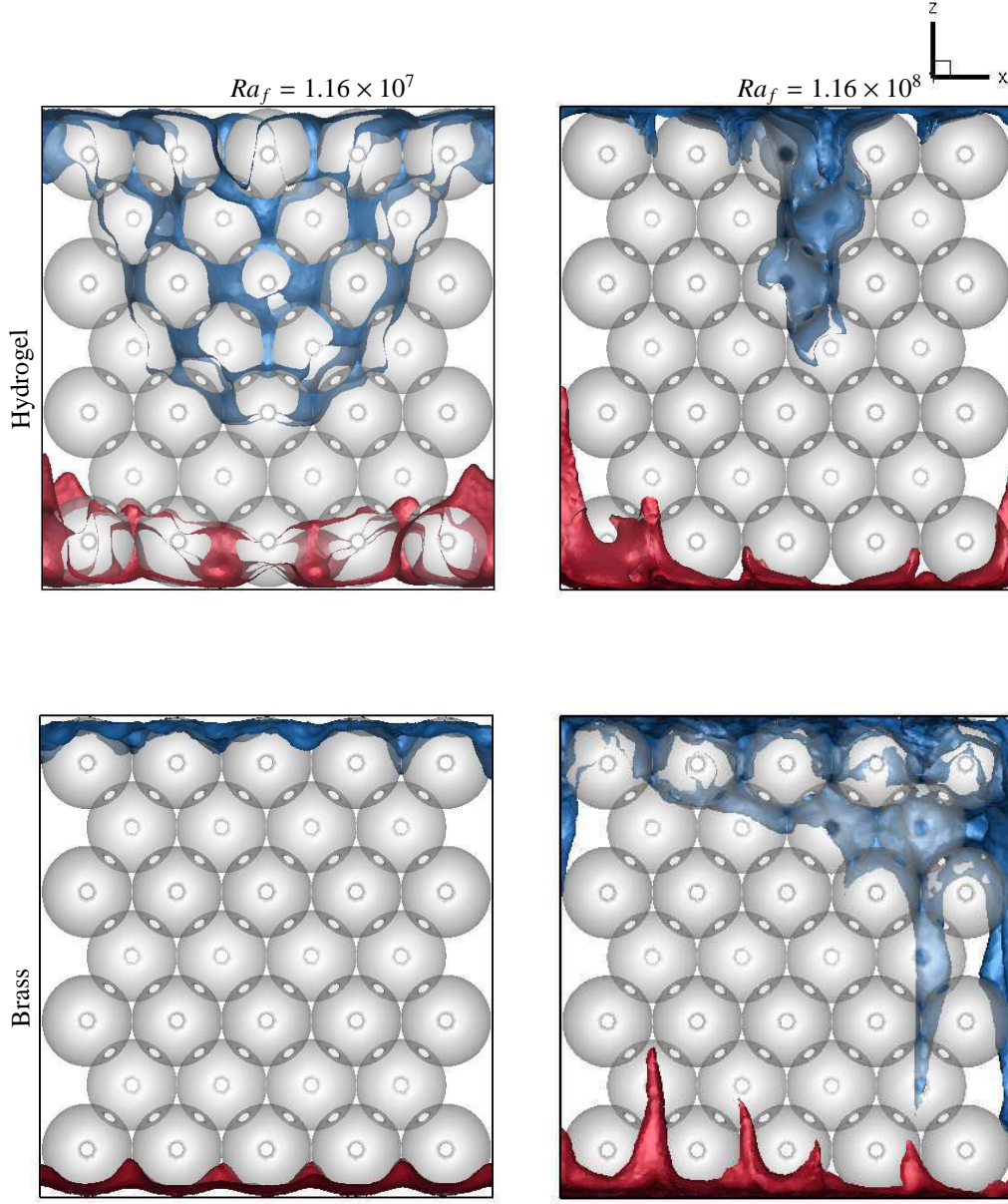
Figure 1: A side-view of the instantaneous non-dimensional temperature isosurfaces at $t/t_0 = 20$, in a cavity filled with hydrogel (top) and brass (bottom) beads at $Ra_f = 1.16 \times 10^7$ (left) and $Ra_f = 1.16 \times 10^8$ (right) ($\Theta^* = 0.2$,Blue; $\Theta^* = 0.8$,Red)

shows isosurfaces of the scaled lateral velocity v^*, i.e. the velocity component in the Y-direction at $t/t_0 = 20$. At low $Ra_f = 1.16 \times 10^7$, lateral flow is almost absent in the brass packed cavity, and mostly concentrated along the walls for the hydrogel packed cavity. At higher $Ra_f = 1.16 \times 10^8$, lateral flow in the core of the hydrogel packed cavity has strongly increased compared to $Ra_f = 1.16 \times 10^7$, resulting in significant lateral velocities throughout the cavity. In the brass filled cavity, even at higher $Ra_f = 1.16 \times 10^8$, lateral flows are concentrated along the walls and mostly absent in the core of the cavity.

The increased vertical and lateral flow velocities, along the walls and in the core of the cavity, as observed at higher Ra_f, cause convective heat transfer by the fluid to dominate over heat conduction in the solid, diminishing the difference of overall Nu_f for low and high conductivity packing materials, with increase in Ra_f.

3.3. Plane averaged features

In Fig.6(a) we show instantaneous scaled velocity magnitudes $U^* = (u^{*2} + v^{*2} + w^{*2})^{0.5}$ averaged over the XY-plane at $t/t_0 = 20$, as a function of Z/L, for both brass packed and hydrogel packed cavities at $Ra_f = 1.16 \times 10^7$ and $Ra_f = 1.16 \times 10^8$. Also included are the same plane averaged velocities for pure Rayleigh-Bénard (RB) convection in a water filled cavity at the same values of Ra_f. Due to the applied scaling, scaled velocities in RB convection are roughly independent of Ra_f. In the packed cavity, however, the scaled velocities strongly depend on Ra_f. At $Ra_f = 1.16 \times 10^7$, the scaled velocities in the hydrogel packed cavity are about an order of magnitude smaller compared to the RB convection, whereas they are yet another order of magnitude smaller in the brass packed cavity. This indicates that, at low Rayleigh numbers, convective heat transfer is small compared to that in RB convection in the hydrogel packed cavity, whereas it is negligible in the brass packed cav-
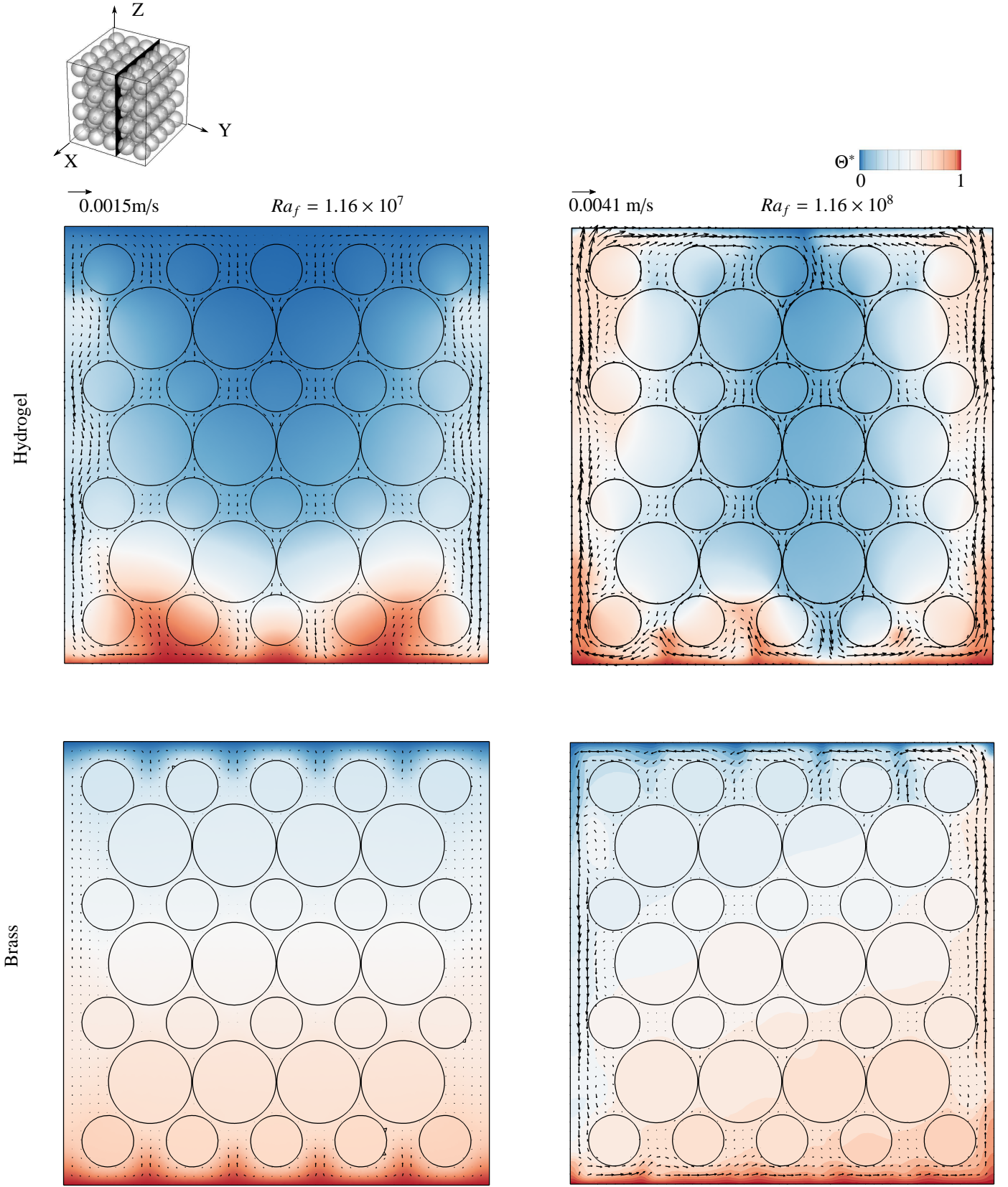
5

Figure 2: Instantaneous velocity vectors and temperatures at $t/t_0 = 20$, in a characteristic vertical plane at $Y/L = 0.62$ at $Ra_f = 1.16 \times 10^7$ (left) and $Ra_f = 1.16 \times 10^8$ (right), for a cavity packed with hydrogel (top) and brass (bottom) beads.
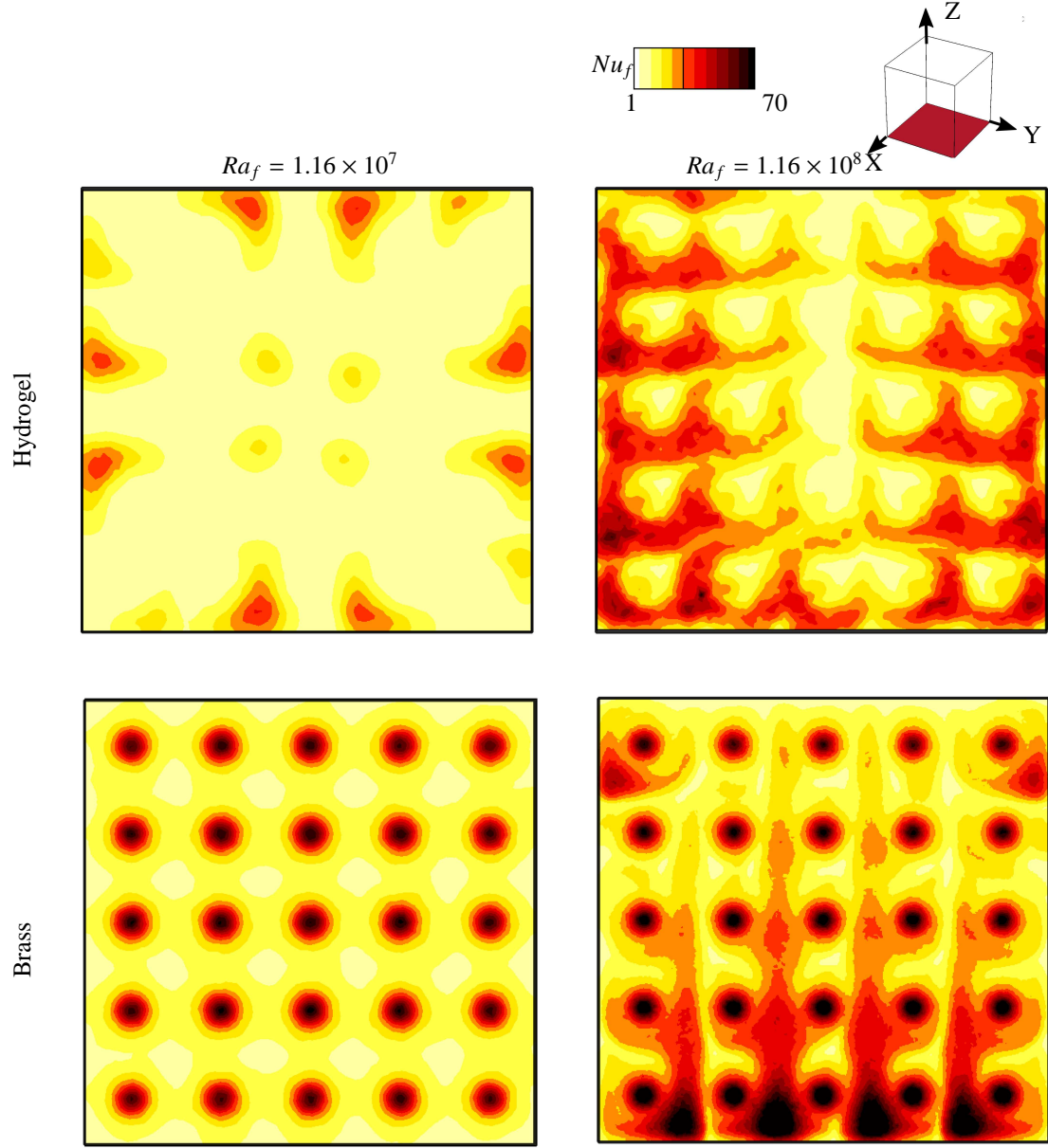
Figure 3: Instantaneous Nusselt number Nu_f distributions at the hot wall at $t/t_0 = 20$, in a cavity packed with hydrogel (top) and brass (bottom) beads, at $Ra_f = 1.16 \times 10^7$ (left) and 1.16×10^8 (right).

ity dominated by conduction. At $Ra_f = 1.16 \times 10^8$, the average velocity magnitudes in the hydrogel and brass packed cavities are similar, and only a factor two lower than in RB convection, confirming that convection starts to dominate the overall heat transfer in packed cavities at higher Rayleigh numbers, causing it to become independent of the packing material and to approach that of RB convection.

In Fig.6(b) we show instantaneous normalized temperatures, averaged over the XY-plane at $t/t_0 = 20$, as a function of Z/L, for both brass packed and hydrogel packed cavities at $Ra_f = 1.16 \times 10^7$ and $Ra_f = 1.16 \times 10^8$. Also included are the same plane averaged temperatures for pure Rayleigh-Bénard (RB)

convection at the same values of Ra_f. At $Ra_f = 1.16 \times 10^7$, the plane averaged temperature in the brass packed cavity varies almost linearly with height, again indicating the dominance of solid conduction heat transfer over convection. In the hydrogel packed cavity on the other hand, the vertical temperature profile is strongly nonlinear due to the significance of convection, exhibiting thermal boundary layers at the isothermal walls that are similar to those in RB convection. In the core of the cavity, however, the temperature varies much more gradually in the hydrogel packed cavity, compared to RB convection. At $Ra_f = 1.16 \times 10^8$, the plane averaged temperatures close to the isothermal walls in the both packed cavities become similar to

$Ra_f = 1.16 \times 10^7$
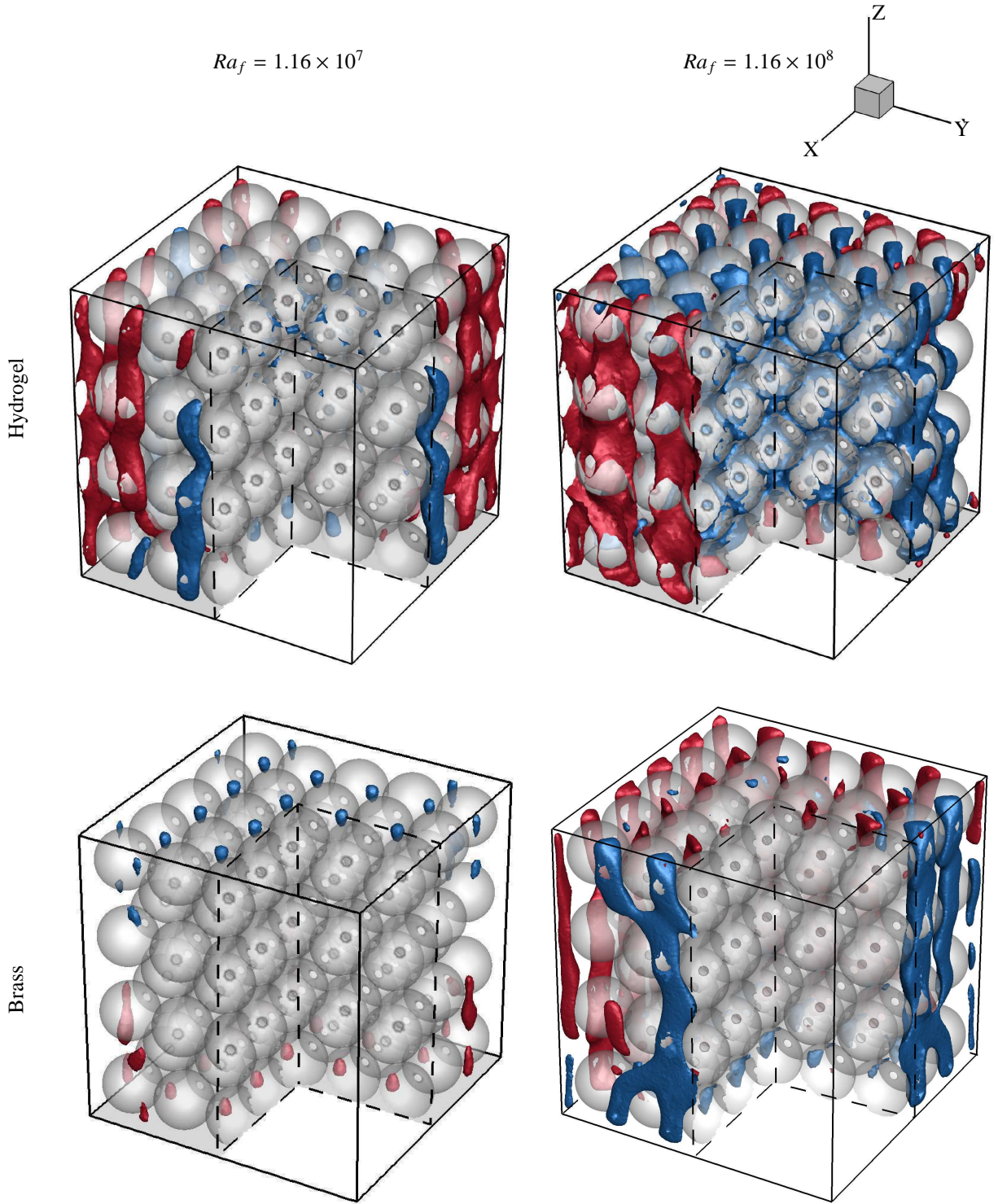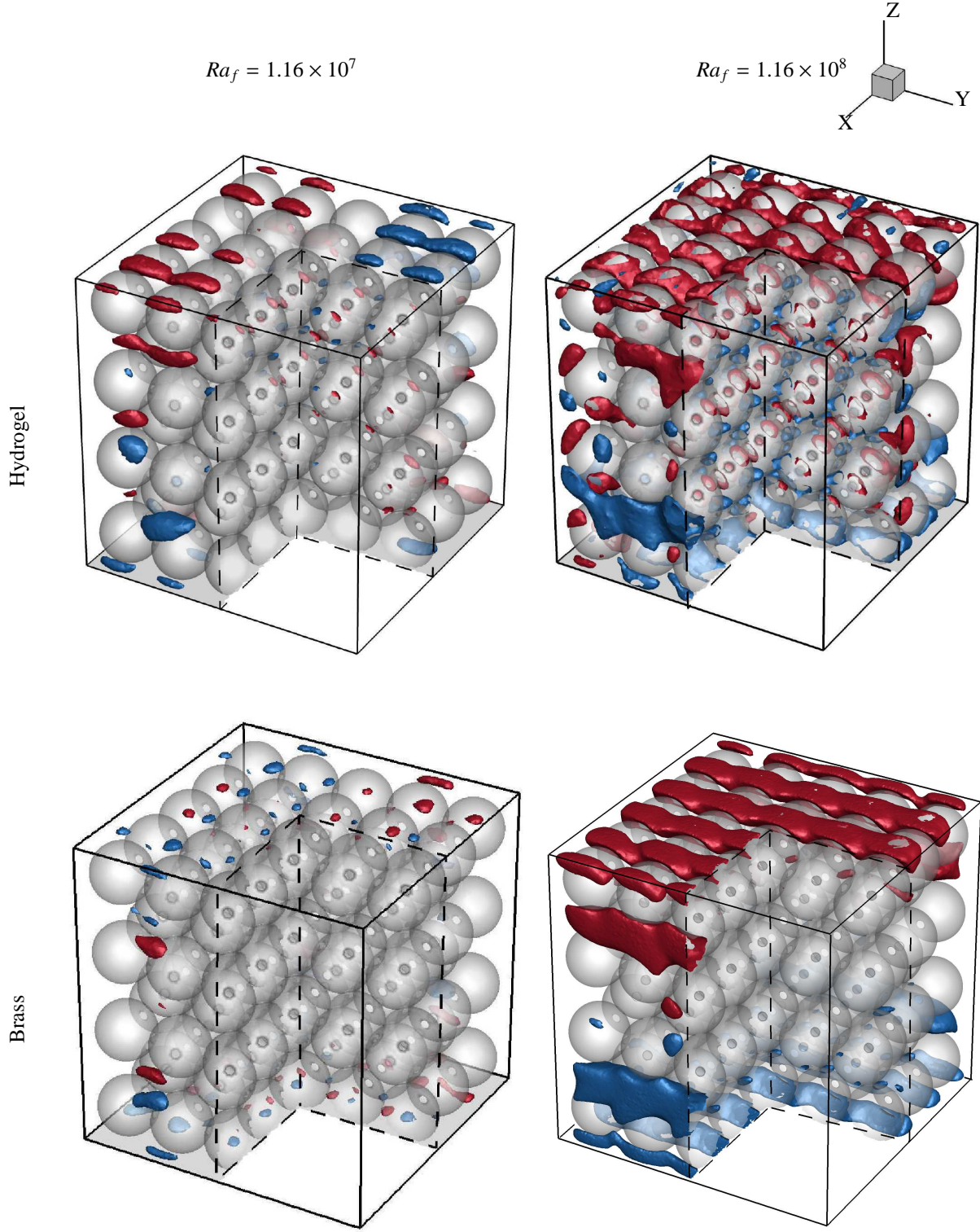
$Ra_f = 1.16 \times 10^8$

Hydrogel

Brass

Figure 4: Instantaneous normalized vertical velocity isosurfaces, $w^* = 0.2$ (red) and $w^* = -0.2$ (blue) at $t/t_0 = 20$, in a cavity packed with hydrogel (top) and brass (bottom) at $Ra_f = 1.16 \times 10^7$ (left) and 1.16×10^8 (right).

those in RB convection, whereas in the core of the cavity the temperature profile is still strongly influenced by the presence of the solid packing.

3.4. The time evolution of wall-averaged heat transfer

In Fig.7 we show the time evolution of the instantaneous, bottom wall-averaged, Nusselt number for cavities packed with brass, steel and hydrogel beads ($\lambda_{brass} > \lambda_{steel} > \lambda_{hydrogel}$) at $Ra_f = 1.16 \times 10^7$ and 1.16×10^8, as well as for RB convection. At the lower $Ra_f = 1.16 \times 10^7$, the solid packing suppress

Figure 5: Instantaneous normalized lateral velocity isosurfaces, $v^* = 0.2$ (red) and $v^* = -0.2$ (blue) at $t/t_0 = 20$, in a cavity packed with hydrogel (top) and brass (bottom) beads at $Ra_f = 1.16 \times 10^7$ (left) and 1.16×10^8 (right).

all flow and thermal fluctuations and the wall heat transfer is steady for all packing materials. In RB convection, on the other hand, significant ($\sim 10\%$ peak-peak) fluctuations in heat transfer are being observed. In the packed cavities, the wall-averaged heat transfer increases with increased solid conductivity, but is always lower than for RB convection, due to the

highly suppressed convection.

At the higher $Ra_f = 1.16 \times 10^8$, flow and heat transfer exhibit oscillatory behaviour, with peak-peak oscillations $\sim 12\%$ in RB convection to $\sim 3\%$ in the brass bead packed cavity. In all cases, however, the wall-averaged heat transfer is statistically steady. Due to the increased role of convection, heat transfer in

9
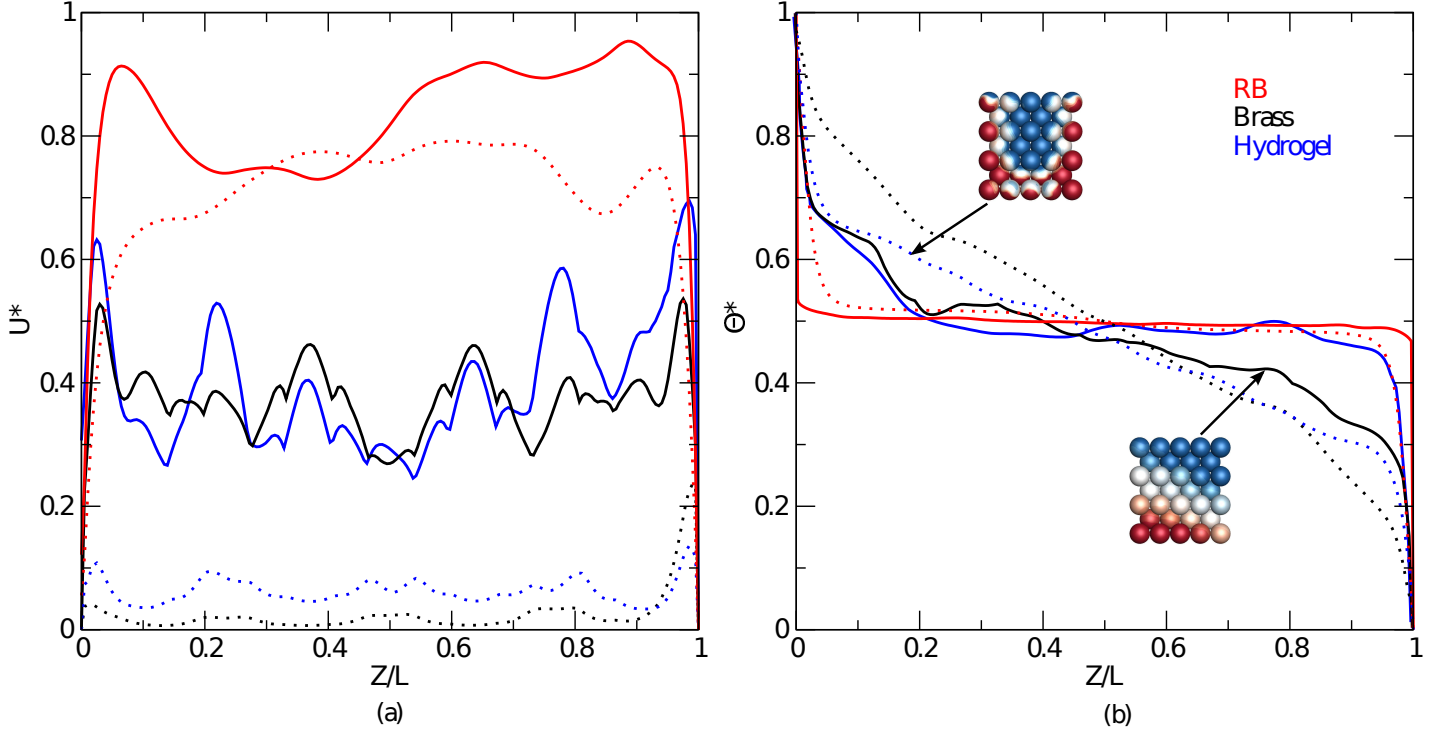
Figure 6: Instantaneous scaled velocity magnitudes U^* (a) and normalized temperatures Θ^* (b) at $t/t_0 = 20$, averaged over XY-planes as a function of Z/L, in RB convection (red), hydrogel packed (blue) and brass packed (black) cavities at $Ra_f = 1.16 \times 10^7$ ($\cdots$) and 1.16×10^8 (—). An example of the temperature distribution on the surface of the solid spheres is depicted in the inset.
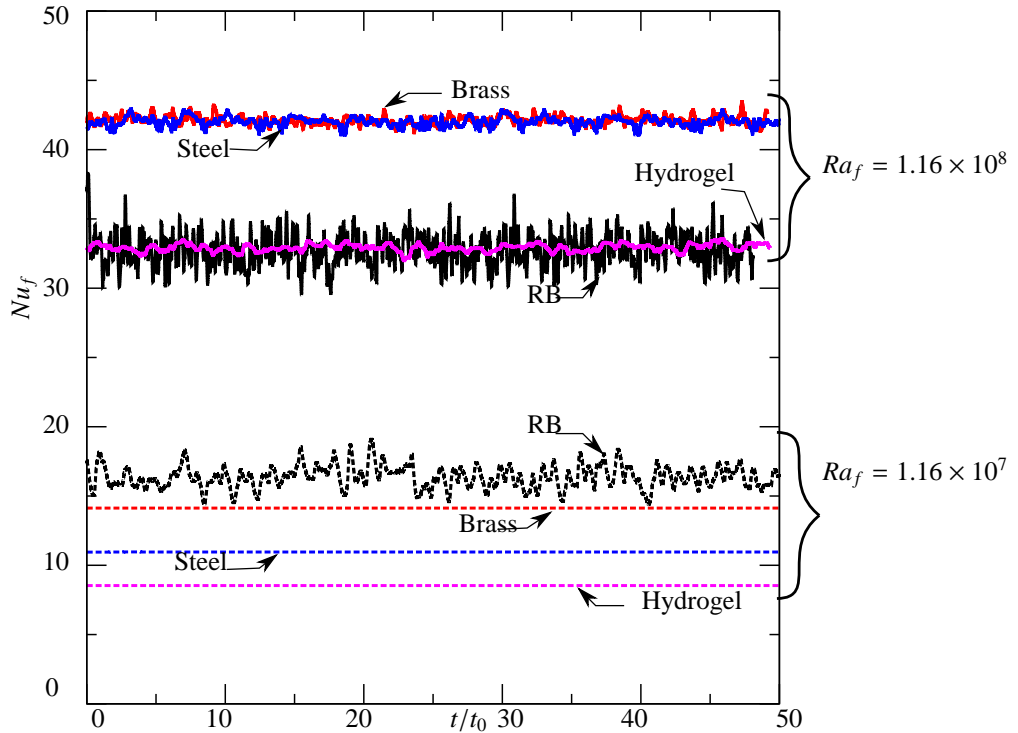

Figure 7: Time evolution of instantaneous, bottom wall-averaged, Nusselt number for cavities packed with brass (red), steel (blue) and hydrogel (magenta) beads, as well as for RB convection (black) at $Ra_f = 1.16 \times 10^7$ (dashed) and 1.16×10^8 (solid).

the hydrogel packed cavity is almost equal to that in RB convection. For the high conductivity brass and steel packing, the conductive heat transfer along with the convective heat transfer, results in wall-averaged Nusselt numbers which are 30% higher

than for the RB convection and hydrogel packed cavities.

3.5. Analysis long-term time-averaged wall heat transfer mechanisms

To understand the influence of thermal properties of the solid packing on heat transfer, we focus on the analysis of time and wall-averaged Nusselt numbers in Fig.8, in which Nusselt numbers obtained from the present simulations and from our experiments in [14] are compared for cavities packed with different materials, as well as fluid only RB convection, at different Ra_f. In Fig.8, the $Nu_f = 0.118 \times Ra_f^{0.3063}$ correlation obtained from our experiments for pure fluid RB convection at $10^7 < Ra_f < 10^8$ is extrapolated towards $Ra_f = 10^6$ for comparison with the packed cavity results at $Ra_f < 10^7$. For the RB convection, and hydrogel and brass packed cavities, Nusselt numbers obtained from simulations are in good agreement with experimental results at $1.16 \times 10^7 \leq Ra_f \leq 1.16 \times 10^8$. At very low $Ra_f \approx 10^6$, heat transfer in steel and brass packed cavities is higher, and in hydrogel and polypropylene (PP) packed cavities is lower, than for the RB convection. As will be discussed in more detail below, at this low Rayleigh number, convection is effectively suppressed due to wall friction in all packings, eliminating convective heat transfer. The addition of a significant amount of solid conduction heat transfer in steel and brass, however, causes overall heat transfer in these packings to be larger than for RB convection. Increasing Ra_f to 10^7 causes an onset of convection and increasing Nusselt numbers in the low conductivity (PP and hydrogel) packings. In the steel and brass packings, on the other hand, convection is still suppressed at $Ra_f \approx 10^7$. As a result, for steel and brass the Nusselt number is fully determined by solid conduction and independent of Ra_f up to $Ra_f \approx 10^7$.

Upon a further increase to $Ra_f \approx 10^8$, convective heat transfer starts to dominate the overall heat transfer in all packings, causing Nusselt numbers to be very similar for brass and steel packings. At $Ra_f \approx 10^8$, the influence of solid conduction can still be observed, causing Nusselt number in steel and brass packings to be higher, and in PP and hydrogel packings to be lower than for RB convection.

To further study the impact of coarse-grained solid packings on the overall heat transfer, the heat transfer enhancement factor E, defined as:

$$E = \frac{Nu_f}{Nu_{RB}} \qquad (7)$$

is used to compare the overall heat transfer in packed cavities to that in an RB convection. When the enhancement factor $E > 1$, the coarse-grained solid packings enhances heat transfer compared to RB convection, whereas for $E < 1$ the coarse-grained solid packings reduces heat transfer.

For high thermal conductivity brass and steel packings, $E > 1$ at low $Ra_f \approx 10^6$. At increased Ra_f, E decreases, reaching a minimum around $Ra_f = 1 - 2 \times 10^7$, after which it increases with increasing Nu_f. For both materials, E appears to approach an asymptotic value around $E = 1.2$ for large Ra_f.

For the low thermal conductivity packings PP and hydrogel, $E < 1$ for the entire range of studied Ra_f. At very low

$Ra_f \approx 10^6$, heat transfer is reduced by an order of magnitude compared to RB convection, due to the suppression of flow and the absence of significant conductive heat transfer. With increasing Ra_f, convective heat transfer increases and the total heat transfer seems to asymptotically approach that for RB convection ($E \to 1$ for $Ra_f \to \infty$).

From the above it is clear that conduction heat transfer plays a dominant role in high conductivity packings at low Rayleigh numbers, whereas convective heat transfer dominates at higher Rayleigh numbers and in low conductivity packings. In order to more precisely quantify the relative contribution of (solid and stagnant fluid) conduction and fluid convection to the total heat transfer, we calculate the effective convective enhancement factor, E_{conv}:

$$E_{\mathrm{conv}} = \frac{Nu_f - Nu_c}{Nu_{RB} - 1} \qquad (8)$$

where, Nu_c is the contribution of solid and (stagnant) fluid conduction to the overall heat transfer in packed cavities. Nu_c was obtained from simulations in which gravity was set to zero, thus leaving solid and stagnant fluid conduction as the only heat transfer mechanisms.

Fig.9 shows that, at low Ra_f, the contribution E_{conv} of convection to the total heat transfer enhancement is almost zero for all packings materials. This may be understood from the fact that convective flow is effectively suppressed due to wall friction in the coarse-grained packings. Thus it is concluded that E being larger than 1 at low at $Ra_f \approx 10^6$ for brass and steel packings is due to the increased thermal conduction, as compared to the situation for a fluid-only filled cavity.

At $Ra_f \approx 10^7$, the contribution E_{conv} of convection to the heat transfer enhancement is significantly less for steel and brass packings, compared to PP and hydrogel packings, with the latter two being almost equal. This indicates that convective flow is very similar in PP and hydrogel packings, whereas it is almost absent in the high conductivity packings. The latter can be understood from the stabilizing effect that the high conductivity packings has on the (no-flow) stratified temperature distribution. For brass and steel packings, even though $E > 1$ at $Ra_f = 1.16 \times 10^8$, E_{conv} is less than 1, and even lower than E_{conv} for PP and hydrogel packings. Apparently, even at this high Rayleigh number, at which convection is the dominant heat transfer mechanism for all packings, the relative contribution of convection to the overall heat transfer is still slightly lower for brass and steel packings, compared to PP and hydrogel packings.

4. Summary and Conclusion

We performed numerical simulations of fluid natural convection in bottom-heated, top-cooled cubical cavities packed with relatively large ($d/L = 0.2$) solid spheres of largely varying thermal conductivities (solid-to-fluid thermal conductivity ratios between 0.3 and 198), focusing on the pore-scale flow and heat transfer, at $1.16 \times 10^6 \leq Ra_f \leq 1.16 \times 10^8$. At low Rayleigh numbers $\leq 10^6$, the packings effectively suppresses
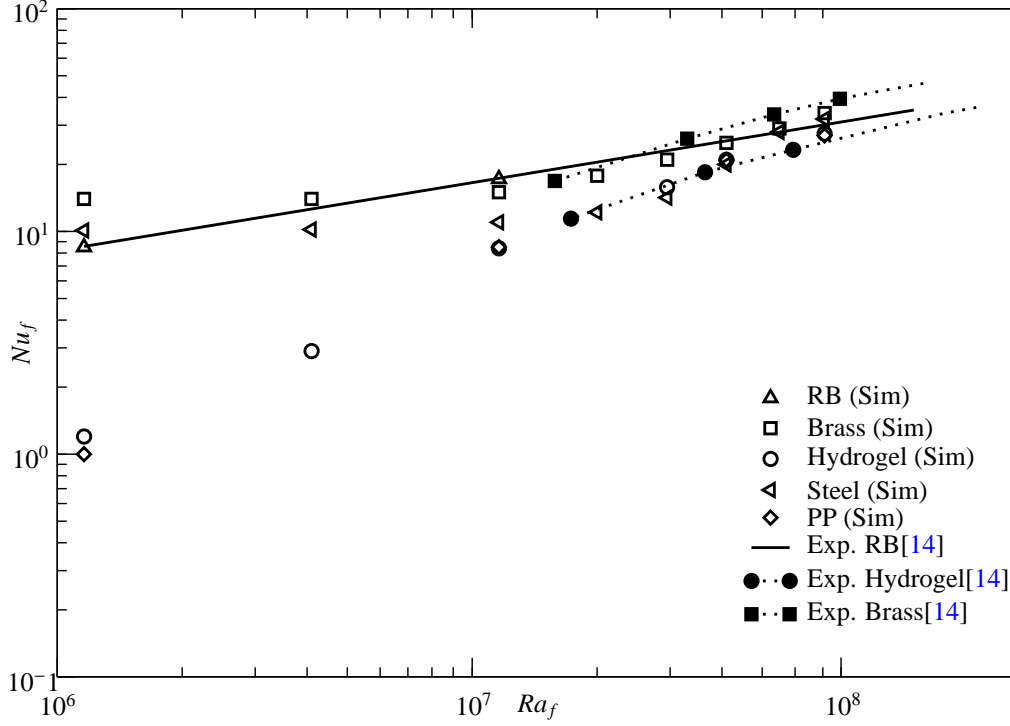
Figure 8: Simulated and experimental long-term time-and-wall-averaged Nusselt numbers as a function of Rayleigh number for $1.16 \times 10^6 \leq Ra_f \leq 1.16 \times 10^8$ in cavities packed with polypropylene (PP), hydrogel, steel and brass, as well as in RB convection. The solid line represents the $Nu_f - Ra_f$ relation obtained experimentally for RB convection and the dotted lines connecting the symbols represent the asymptotic behavior of Nu_f with increase in Ra_f for different packing materials.
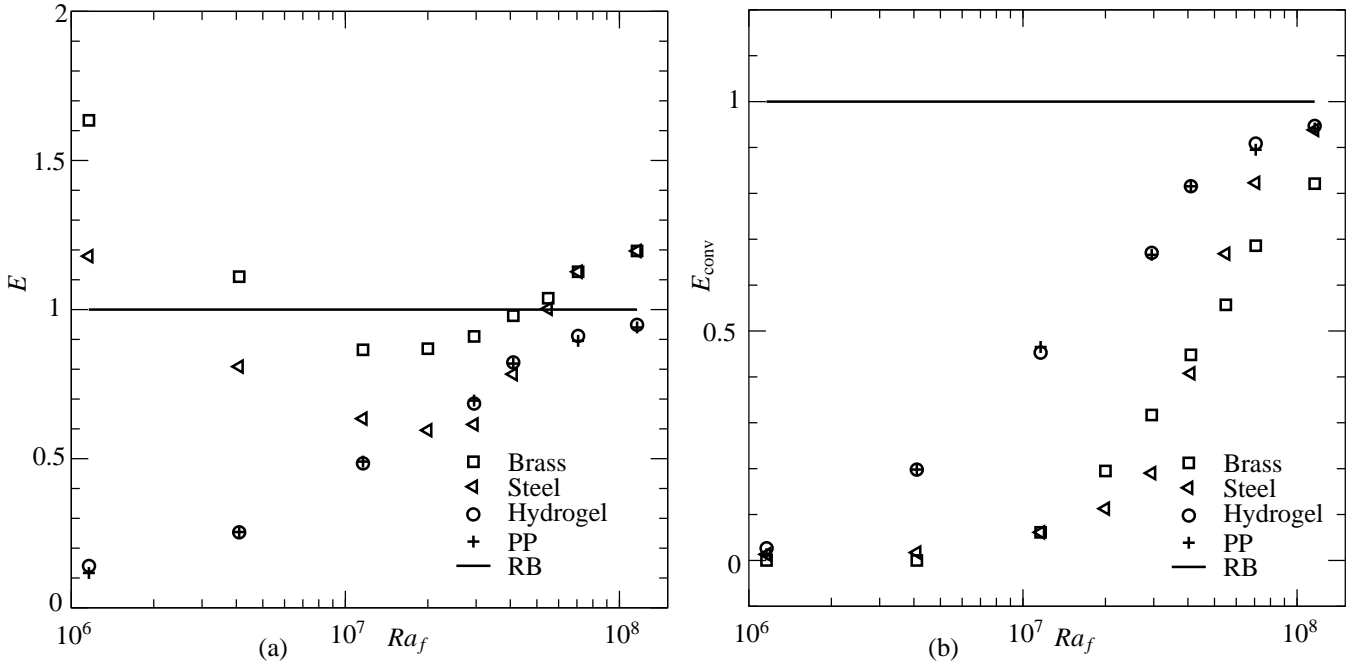

Figure 9: Heat transfer in a cavity packed with PP, hydrogel, steel and brass (a) scaled total heat transfer (b) scaled convective heat transfer.

convective heat transfer, irrespective of the packings material. As a result, the overall heat transfer is strongly reduced in low conductivity packings, as compared to pure Rayleigh-Bénard convection in a fluid-only filled cavity. For high conductivity solid packings, however, the overall heat transfer is increased compared to RB convection, due to a significant contribution of conductive heat transfer. At intermediate Rayleigh numbers $\approx 10^7$, low conductivity coarse-grained packings no longer suppress convection. High conductivity packings, on the other hand, have a strongly stabilizing effect on the (stagnant) strati-

12

fied temperature distribution that would be present in e.g. zero gravity, and as a result, convective flow is still highly suppressed. Consequently, at intermediate Rayleigh numbers, the total heat transfer is lower than for RB convection, even in high conductivity packings.

With an even further increase of Rayleigh number $> 10^8$, convection starts to be the dominant heat transfer mechanism in packed cavities, irrespective of the packings material. As a consequence, convective heat transfer for all packings is close to that for RB convection, although the contribution of solid conduction in high conductivity packings causes the overall heat transfer to be above that for RB convection. These results help us to understand the mechanism of heat transfer in a porous media filled cavity with different packing materials.

The results presented in this paper have been obtained for mono-sized, relatively large (d/L = 0.2) packings of solid spheres. For such coarse packings, the overall flow strongly deviates from Darcy flow. The influence of sphere size on the trends observed in this paper, e.g. on the Rayleigh number at which the overall heat transfer is no longer influenced by the presence of the solid packing, yet remains to be further studied, as is the transition from non-Darcy to Darcy behavior at shrinking sphere sizes. The influence of a multi-sized distribution of the sphere sizes of the packing was also beyond the scope of the present paper, but is a very interesting topic for further study. A lower porosity, resulting from the presence of spheres of varying size, close to the vertical walls might lead to a lower heat transfer, especially at low and intermediate Rayleigh numbers at which the convective flow is concentrated along the vertical walls.

Acknowledgments

Appendix A. Validation of solver

To validate our newly developed OpenFOAM solver "boussinesqChtMultiRegionFoam", we compared results obtained with this solver for a natural convection conjugate heat transfer problem to previously published results obtained using a control volume based finite difference method [28] and with a boundary element method [29]. The studied 2-dimensional problem is illustrated in Fig.A.10. It consists of natural convection in a square $L \times L$ cavity. Adjacent to the left cavity wall there is a $0.2 \times L$ thick layer of solid material, which is heated from the left. The right side wall of the cavity is cooled. The top

and bottom walls are adiabatic. The origin of the geometry is taken at the lowest point of the fluid-solid interface. We used a 100×100 equidistant mesh spacing, with the solver and numerical settings as described in section 2.2. We used a transient solver, but the flow reached a steady state after an initial transient of approximately 15 turnover times. Time averaged results were obtained by averaging over a period of 20 turn-over times after the steady state had been reached. Two cases, with the thermal conductivity ratio of the solid wall to the fluid, λ_s/λ_f=1 and λ_s/λ_f=10, are studied for a Grashof number $Gr = 10^7$ and Prandtl number, Pr = 0.7. Values of non-dimensional temperature (Θ^*) and non-dimensional heat flux (Q) at the left solid-fluid interface are reported in Fig.A.11 and Fig.A.12, respectively, and compared to the results reported in [28, 29] . We obtain a fair agreement (differences in temperatures less than 5% and differences in heat flux less than 10%) with the results by Hriberšek and Kuhn [29], that were obtained with a boundary element method . We see a very good agreement (differences in temperatures less than 1% and differences in heat flux less than 3%) with the results by Kaminski [28] that were obtained with a steady-state control volume based finite difference method.
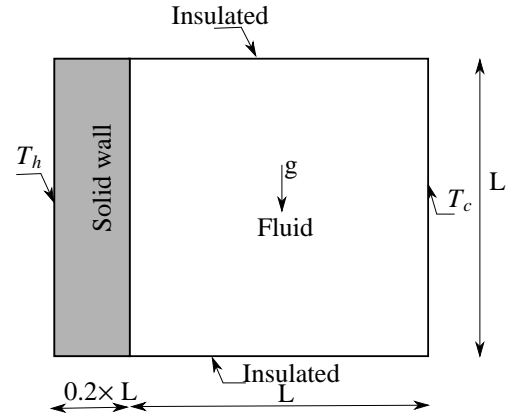

Figure A.10: Schematic representation: Conjugate heat transfer with horizontal temperature gradient.

References

[1] D. J. Goering, P. Kumar, Winter-time convection in open-graded embankments, Cold Regions Science and Technology 24 (1) (1996) 57–74. doi:10.1016/0165-232X(95)00011-Y.

[2] A. Mohamad, Heat transfer enhancements in heat exchangers fitted with porous media part I: constant wall temperature, International Journal of Thermal Sciences 42 (4) (2003) 385–395. doi:10.1016/s1290-0729(02)00039-x.

[3] D. J. Gunn, Transfer of heat or mass to particles in fixed and fluidised beds, International Journal of Heat and Mass Transfer 21 (4) (1978) 467–476. doi:10.1016/0017-9310(78)90080-7.

[4] M. Mesgarpour, A. Heydari, S. Saedodin, Numerical analysis of heat transfer and fluid flow in the bundle of porous tapered fins, International Journal of Thermal Sciences 135 (2019) 398–409. doi:10.1016/j.ijthermalsci.2018.09.032.

[5] S. Ueda, S. Natsui, H. Nogami, J.-I. Yagi, T. Ariyama, Recent progress and future perspective on mathematical modeling of blast furnace, ISIJ International 50 (7) (2010) 914–923. doi:10.2355/isijinternational.50.914.
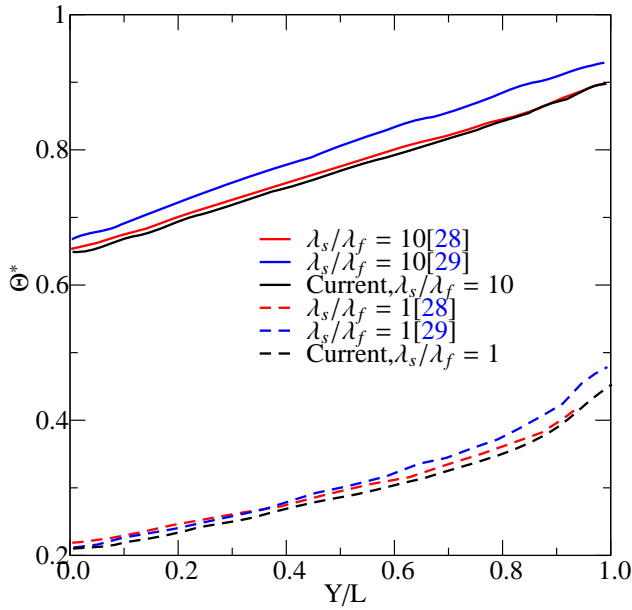
Figure A.11: Non-dimensional temperature, Θ^* between the solid and fluid interface along the vertical at $Gr = 10^7$ for $\lambda_s/\lambda_f = 1, 10$.
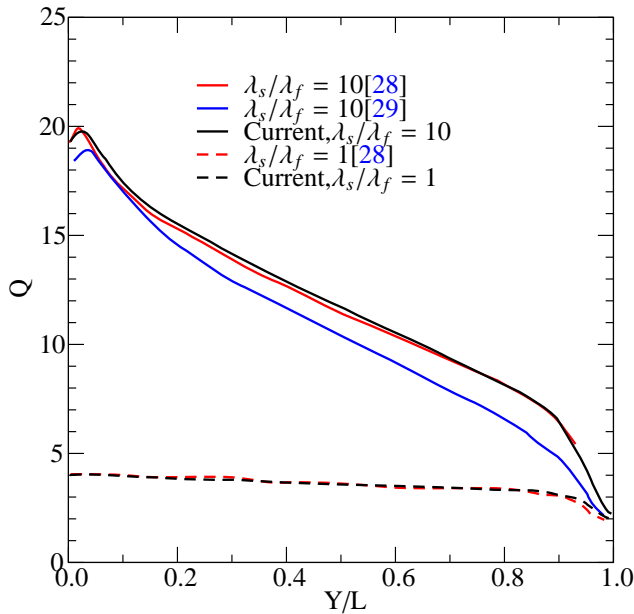

Figure A.12: Non-dimensional heat flux, Q between the solid and fluid interface along the vertical at $Gr = 10^7$ for $\lambda_s/\lambda_f = 1, 10$.

[6] H.-J. Diersch, O. Kolditz, Variable-density flow and transport in porous media: approaches and challenges, Advances in water resources 25 (8-12) (2002) 899–944. doi:https://doi.org/10.1016/S0309-1708(02)00063-5.

[7] D. A. Nield, A. Bejan, Convection in Porous Media, Springer New York, 2013. doi:10.1007/978-1-4614-5541-7.

[8] N. Kladias, V. Prasad, Natural Convection in Horizontal Porous Layers: Effects of Darcy and Prandtl Numbers, Journal of Heat Transfer 111 (4) (1989) 926–935. doi:10.1115/1.3250807.

[9] N. Kladias, V. Prasad, Flow Transitions in Buoyancy- Induced Non-Darcy Convection in a Porous Medium Heated From Below, Journal of Heat Transfer 112 (1990) 675–684.

[10] M. S. Phanikumar, R. L. Mahajan, Non-Darcy natural convection in high porosity metal foams, International Journal of Heat and Mass Transfer 45 (18) (2002) 3781–3793. doi:10.1016/S0017-9310(02)00089-3.

[11] H. Sakamoto, F. A. Kulacki, Buoyancy Driven Flow in Saturated Porous Media, Journal of Heat Transfer 129 (6) (2007) 727. doi:10.1115/1.2717937.

[12] D. J. Keene, Thermal Convection in Porous Media at High Rayleigh Numbers, Journal of Heat Transfer 137 (2015) 1–4. doi:10.1115/1.4029087.

[13] C. R. B. Lister, An explanation for the multivalued heat transport found experimentally for convection in a porous medium, Journal of Fluid Mechanics 214 (1990) 287–320. doi:10.1017/S0022112090000143.

[14] I. Ataei-Dadavi, M. Chakkingal, S. Kenjeres, C. R. Kleijn, M. J. Tummers, Flow and heat transfer measurements in natural convection in coarse-grained porous media, International Journal of Heat and Mass Transfer 130 (2019) 575–584. doi:10.1016/j.ijheatmasstransfer.2018.10.118.

[15] T. Jonsson, I. Catton, Prandtl number dependence of natural convection in porous media, Journal of Heat Transfer 109 (2) (1987) 371. doi:10.1115/1.3248090.

[16] V. Kathare, J. H. Davidson, F. A. Kulacki, Natural convection in water-saturated metal foam, International Journal of Heat and Mass Transfer 51 (15-16) (2008) 3794–3802. doi:10.1016/j.ijheatmasstransfer.2007.11.051.

[17] H. Xu, Z. Xing, The lattice Boltzmann modeling on the nanofluid natural convective transport in a cavity filled with a porous foam, International Communications in Heat and Mass Transfer 89 (2017) 73–82. doi:10.1016/j.icheatmasstransfer.2017.09.013.

[18] C. Y. Zhao, T. J. Lu, H. P. Hodson, Natural convection in metal foams with open cells, International Journal of Heat and Mass Transfer 48 (12) (2005) 2452–2463. doi:10.1016/j.ijheatmasstransfer.2005.01.002.

[19] C. Zhao, L. Dai, G. Tang, Z. Qu, Z. Li, Numerical study of natural convection in porous media (metals) using lattice boltzmann method (LBM), International Journal of Heat and Fluid Flow 31 (5) (2010) 925–934. doi:10.1016/j.ijheatfluidflow.2010.06.001.

[20] B. Blais, F. Bertrand, On the use of the method of manufactured solutions for the verification of CFD codes for the volume-averaged Navier-Stokes equations, Computers and Fluids 114 (2015) 121–129. doi:10.1016/j.compfluid.2015.03.002.

[21] I. Thiagalingam, M. Dallet, I. Bennaceur, S. Cadalen, P. Sagaut, Exact non local expression for the wall heat transfer coefficient in tubular catalytic reactors, International Journal of Heat and Fluid Flow 54 (2015) 97–106. doi:https://doi.org/10.1016/j.ijheatfluidflow.2015.03.007.

[22] R. W. Johnson, Handbook of fluid dynamics, Crc Press, 2016.

[23] D. D. Gray, A. Giorgini, The validity of the Boussinesq approximation for liquids and gases, International Journal of Heat and Mass Transfer 19 (5) (1976) 545–551. doi:10.1016/0017-9310(76)90168-X.

[24] H. G. Weller, G. Tabor, H. Jasak, C. Fureby, A tensorial approach to computational continuum mechanics using object-oriented techniques, Computers in Physics 12 (6) (1998) 620–631. doi:10.1063/1.168744.

[25] J. Finn, S. V. Apte, Relative performance of body fitted and fictitious domain simulations of flow through fixed packed beds of spheres, International Journal of Multiphase Flow 56 (2013) 54–71. doi:10.1016/j.ijmultiphaseflow.2013.05.001.

[26] A. Zenklusen, S. Kenjereš, P. R. von Rohr, Vortex shedding in a highly porous structure, Chemical Engineering Science 106 (2014) 253–263. doi:https://doi.org/10.1016/j.ces.2013.11.022.

[27] A. Zenklusen, S. Kenjereš, P. R. von Rohr, Mixing at high schmidt number in a complex porous structure, Chemical Engineering Science 150 (2016) 74–84. doi:https://doi.org/10.1016/j.ces.2016.04.057.

[28] D. Kaminski, C. Prakash, Conjugate natural convection in a square enclosure: effect of conduction in one of the vertical walls, International Journal of Heat and Mass Transfer 29 (12) (1986) 1979–1988. doi:10.1016/0017-9310(86)90017-7.

[29] M. Hriberšek, G. Kuhn, Conjugate heat transfer by boundary-domain integral method, Engineering Analysis with Boundary Elements 24 (4) (2000) 297–305. doi:10.1016/S0955-7997(00)00008-4.

[30] R. Issa, Solution of the implicitly discretised fluid flow equations by operator-splitting, Journal of Computational Physics 62 (1) (1986) 40 – 65. doi:https://doi.org/10.1016/0021-9991(86)90099-9.

[31] O. Shishkina, R. J. A. M. Stevens, S. Grossmann, D. Lohse, Boundary layer structure in turbulent thermal convection and its consequences for the required numerical resolution, New Journal of Physics 12 (7) (2010) 075022.

[32] B. Castaing, G. Gunaratne, F. Heslot, L. Kadanoff, A. Libchaber, S. Thomae, X.-Z. Wu, S. Zaleski, G. Zanetti, Scaling of hard thermal turbulence in Rayleigh-Bénard convection, Journal of Fluid Mechanics 204 (-1) (1989) 1. `doi:10.1017/s0022112089001643`.